Estimation of blade loads for a variable pitch vertical axis wind turbine from particle image velocimetry

LeBlanc, Bruce; Ferreira, Carlos

DOI
10.1002/we.2674

Publication date
2021

Document Version
Final published version

Published in
Wind Energy

Citation (APA)
LeBlanc, B., & Ferreira, C. (2021). Estimation of blade loads for a variable pitch vertical axis wind turbine from particle image velocimetry. *Wind Energy*, *25*(2), 313-332. https://doi.org/10.1002/we.2674

Received: 2 February 2021 | Revised: 19 May 2021 | Accepted: 21 June 2021

DOI: 10.1002/we.2674

RESEARCH ARTICLE

WILEY

Estimation of blade loads for a variable pitch vertical axis wind turbine from particle image velocimetry

Bruce LeBlanc | **Carlos Ferreira**

Wind Energy, Delft University of Technology, Delft, South Holland, Netherlands

Correspondence
Bruce LeBlanc, Wind Energy, Delft University of Technology, Kluyverweg 1, 2629HS Delft, South Holland, Netherlands.
Email: b.p.leblanc@tudelft.nl

Funding information
Arkom Tulyp Wind RVO Netherlands; S4VAWT TKI Wind Op Zee; TKI Wind op Zee; Arkom-Tulyp

Abstract

This paper presents the flow fields and aerodynamic loading of a two bladed H-type vertical axis wind turbine with active variable pitch for load and circulation control. Particle Image Velocimetry is used to capture flow fields at six azimuthal positions of the blades during operation, three upwind and three downwind. Flow phenomena such as dynamic stall and tower shadow are captured in the flow fields. The phase-averaged velocity fields and their time and spatial derivatives are used to calculate the normal and tangential loading at each position for each pitching configuration using the Noca formulation of the flux equations. The results show the effect of load shifting from the upwind to downwind region of the actuator using pitch and the effects of dynamic stall on the blades. The results also provide an unique database for model validation.

KEYWORDS

active pitch control, circulation control, Darrieus VAWT, flow visualization, particle image velocimetry, vertical axis wind turbine

1 | INTRODUCTION

The blades of a vertical axis wind turbine undergo a variety of complex aerodynamic loading fluctuations throughout each rotation: large angle of attack swings, unsteady flow, dynamic stall, blade vortex interaction, and tower shadow to name a few known examples. This leads to many inherent difficulties for designers to properly characterize the loads and performance of these turbines, especially in understanding fatigue. Research interest has increased in the areas of active variable pitch for improving power extraction, controlling the direction of the wake, or minimizing loads.[1–5] In order to provide better insight into these phenomena, a set of flow field measurements through Particle Image Velocimetry were conducted using the PitchVAWT active pitch turbine at Delft University of Technology. This paper presents these flow fields as well as the aerodynamic forces acting on the VAWT blade mid-span section for several upwind and downwind azimuthal positions.

There is a lack of high-quality experimental data for both flow fields and loading phenomena in operation of VAWTs which can be used for calibration and validation of computational models. A review of experimental results available for vertical axis wind turbines was published by Battisti et al[6] which highlighted some gaps in the available literature on experimental campaigns, in particular the difference in Troposkien vs. H-shaped vertical axis turbines. A set of studies was performed by Ferreira,[7] which presented an array of simulations and particle image velocimetry measurements which focused on the near wake of the turbine but also characterized dynamic stall and blade loading with studies using the velocity data captured through both CFD and PIV. Castelein et al[8,9] studied VAWT loading in dynamic stall using a similar PIV technique along with calculation of loads using the Noca flux method. Greenblatt et al[10] looked into dynamic stall specifically with a goal to control the stall behavior with the use of plasma actuators. Other works have focused on the behavior of small VAWTs specifically while looking into the differing stall behavior

---

at multiple tip speed ratios.[11] A detailed study was also performed on the wake of a fixed pitch VAWT in operation by Tescione et al,[12] which provides excellent insight into the wake behavior of the VAWT but doesn't look into the blade level loading phenomena. An example of using PIV for loads measurement in horizontal axis wind turbines in uniform and yawed flow is the work of del Campo et al.[13,14]

The experimental Vertical Axis Wind Turbine studied in this work, referred to as the PitchVAWT, has been designed to test active pitch control systems for VAWTs while providing operational data for thrust loading, normal load measurements, and operating torque. The design of the turbine, along with measurement data studying the effect of active dynamic pitch, can be seen in LeBlanc and Ferreira.[3,15,16]

This work provides a set of data for multiple pitch configurations with a rotor solidity similar to larger scale turbine designs such as the one presented in the S4VAWT project presented in Huijs et al.[1] Detailed velocity fields are given highlighting dynamic stall in both the upwind and downwind portions of the rotation with changing pitch angles. Tower shadow, blade vortex interaction, and in some cases deep stall are shown in the downwind blade pass. Aerodynamic loading is calculated using the approach of Noca[17] for cases both upwind and downwind showing the effects of varying the fixed pitch on both normal and tangential loading. All data cited in this work are available in online in a dataset collection hosted by 4TU.ResearchData.[18]

2 | METHODS

2.1 | Definition of coordinate systems

The coordinate system is given in Figure 1. The turbine is mounted in the wind tunnel such that the incoming flow consistently comes from the 90° azimuth position, with the *x* direction following the direction of the wind. The turbine rotates counterclockwise, and the *y* direction is defined using the right-hand rule.

The blade pitch, β, sign convention is given in Figure 2. The path of the airfoil is shown with a dashed line. Positive turbine pitch is defined as pitching the leading edge towards the center of rotation, which corresponds to an increase in angle of attack for each azimuth position. Negative blade pitch therefore corresponds to a decrease in α.

2.2 | PitchVAWT turbine overview

The PitchVAWT turbine is a two-bladed H-shaped vertical axis turbine with individual pitch control. Two horizontal struts are used per blade located at approximately 25% and 75% of the blade length to minimize deflection during operation. Dimensions of the turbine are shown in Figure 3, and the specifications are given in Table 1. Data are collected from a set of sensors on the turbine measuring azimuth position, rotor torque, thrust load transferred to the tower base, and normal blade loading. Data are collected, processed, and stored using National Instruments™hardware at a rate of 500 Hz. The PitchVAWT turbine is shown in Figure 5. More detail on the design is given for the PitchVAWT turbine in previous works.[15,16] The pitch of each blade of the turbine is controlled by an independent motor and can therefore be configured to test most conceivable pitch schemes in the relatively controlled environment of the OJF.

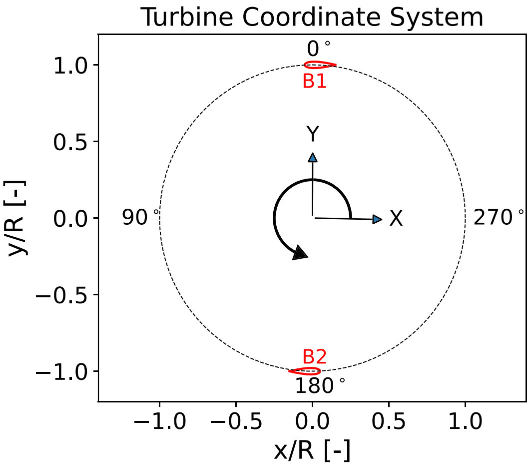

FIGURE 1 Turbine coordinate system, wind approaches from 90° [Colour figure can be viewed at wileyonlinelibrary.com]

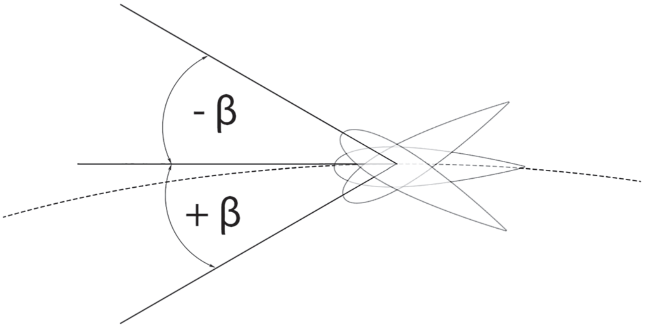

FIGURE 2 Blade pitch convention

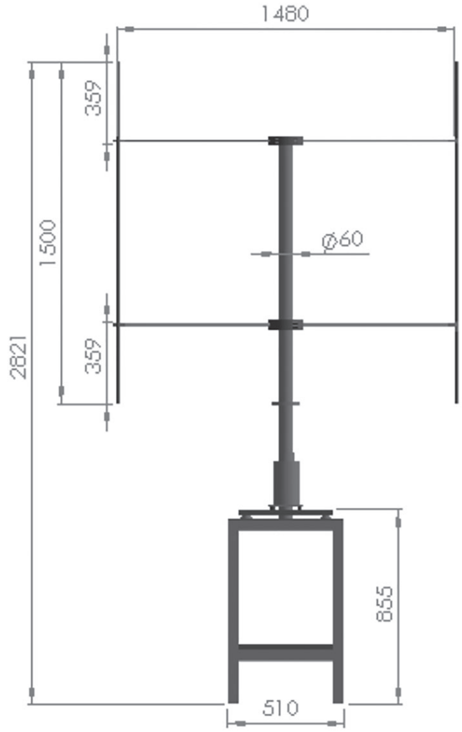

FIGURE 3 PitchVAWT dimensions

TABLE 1 PitchVAWT design specifications

Property	Dimension
NBlades	2
NStruts	4
Rotor height	1.508 m
Diameter	1.48 m
Blade chord	0.075 m
Strut chord	0.060 m
Solidity	0.1
Blade airfoil	NACA0021
Strut airfoil	NACA0018
Blade pitch axis	48% c
Operating λ at $U = 4$ m s^{-1}	1 to 4

2.3 | Wind tunnel facility

Testing of the turbine was conducted in the open jet facility at TU Delft, referred to as OJF. The tunnel is a closed loop open jet test section facility with a 2.85 m × 2.85 m hexagonal cross-section opening into a 13 m long, 8 m high test section. A schematic showing the layout of the OJF is given in Figure 4. The tunnel is capable of a wind speed up to 35 m s^{-1}. A large blue lifting base is available in the tunnel for mounting test hardware. The turbine is mounted to this platform and placed to align in the center of the jet, with the center of the turbine 2 m from the outlet face. A view of the turbine installed in the facility along with the PIV system is given in Figure 5.

2.4 | Test campaign

The wind speed was held to 4 m s^{-1} using the wind tunnel control system, and the turbine rotational speed was controlled via a DC motor controller to be 208 rev/min, for a constant tip speed ratio of 4. Images were taken using two planar PIV fields overlapping around the airfoil in order to capture a complete velocity field surrounding the blades at each position. A 5 V TTL trigger pulse is output by the turbine each rotation at $\theta = 0^\circ$. The TTL pulse is achieved by powering an optical sensor reading a target aligned at the $\theta = 0^\circ$ position with a function generator. Using this signal and the measured rotational speed, a phase locked delay can be calculated. This delay is added to the triggering mechanism in order to capture the data with blade 1 at the correct azimuth position. In order to prevent the effect of laser shadow blocking half of the field of view, two lasers were used to light the area and are synchronized by splitting the TTL trigger pulse. The images are taken at the mid-plane of the rotor in order to minimize any three-dimensional effects by the blade tip vortices or the struts. The cameras are mounted to a computer controlled traverse system which allows the measurement field of view, FOV, to be properly aligned to capture a series of positions in the x-y plane. The

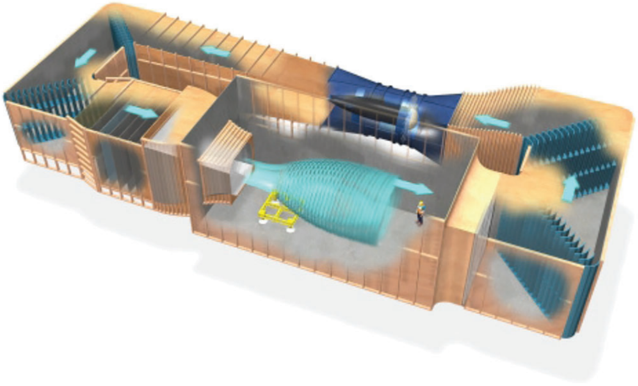

FIGURE 4 Schematic of Open Jet Facility at TU Delft [Colour figure can be viewed at wileyonlinelibrary.com]

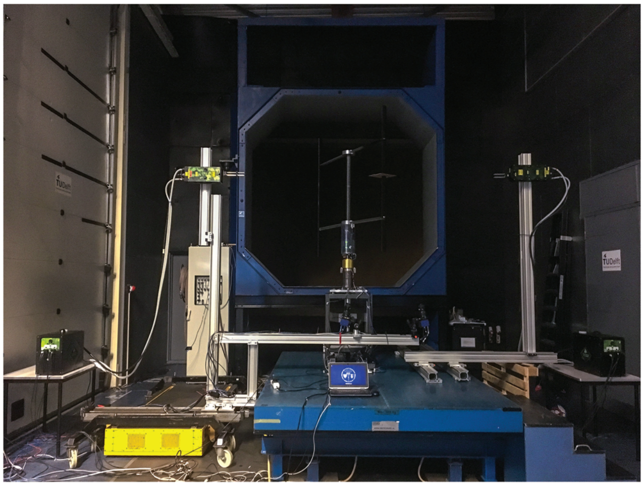

FIGURE 5 PitchVAWT mounted in the Open Jet Facility with opposing synchronized PIV lasers, cameras, and traversing system [Colour figure can be viewed at wileyonlinelibrary.com]

traverse system monitors the general positioning of the local measurement FOV in the global coordinate system. Any small deviations which can be accumulated due to runout of the traverse system or any other unaccounted for motion are corrected for by aligning the expected airfoil position in the global coordinate frame with the measured trailing edge of the airfoil during operation.

The cameras used are LAVision 16 Mpix cameras with 60 mm Nikon Micro-Nikkor lenses using a 2X multiplier zoom lens, giving an overall focal length of 120 mm and an F-Stop of 5.6. Two Evergreen dual pulse PIV lasers were used with the Δt offset between each laser pulse as 0.2 s. A set of 75 images was taken by each camera at each measurement position. A mask is applied to each image to minimize effects of laser reflection on the blade surface as well areas of the blade which obstruct the view of the flow. The raw images are then filtered to remove background noise and enhance the particles. The velocity field is calculated using sequential PIV within LAVision's Davis software. An average and standard deviation of each measurement field are calculated for each position. The calculated fields are then filtered to remove any excessive standard deviation in the measurement vector, usually due to insufficient particles or excessive background noise.

Six azimuths are measured in this experiment, three upwind, and three downwind. All data presented here are in the global reference frame. For each local station around the azimuth, three sets of images are taken: a nominal θ position and two neighboring points with an offset of about $\pm\Delta\theta = 5^\circ$. As the camera system is triggered by a time-delay, any minor deviations in the rotational speed or triggering delays cause a slight deviation in actual angle of measurement. This is accounted for by fitting the transformed raw images with a representation of the airfoil overlaid numerically. The measured azimuth position is then used as the reference location. This is necessary for the calculation of the aerodynamic load as discussed in Section 2.5. Data are collected in three fixed-pitch configurations for the turbine, 0°, 5°, and -5°. The azimuth positions of each local measurement is given Table 2.

The velocity fields are measured at the mid-plane of the rotor disk in order to minimize any three-dimensional effects of the flow. Figure 6 shows a model of the rotor with velocity fields measured for cases $\theta = 90^\circ$ and $\theta = 270^\circ$.

2.5 | Load calculations with Noca method

The experimental velocity fields discussed in Section 3.1 are used to calculate the blade normal and tangential loading for each measurement position. The loads are calculated using the flux formulation described by Noca.[17,19] Originally derived from the conservation of momentum, the method allows for the calculation of body forces in the flow using only the velocity fields and their derivatives. Ferreira used this technique with simulated PIV data[20] discussing the accuracy of the method along with routine issues that are encountered when performing the measurements in the wind tunnel, such as overlapping flow fields from multiple cameras. It was also implemented by Castelein[8] on a VAWT for the study of loading in dynamic stall and by del Campo et al[13,14] while studying loading on a HAWT. This section discusses the implementation of the flux equation and the corrections made for the acceleration of the airfoil body due to rotation. A quick study is shown documenting the sensitivity of the load calculation to the selection of the control surface boundary, including when it doesn't encompass the airfoil, and the specifics of the velocity, acceleration, and vorticity fields used for a calculation for the normal and tangential loading are given for the $\theta = 120^\circ$ azimuthal position.

Noca proposed the following formulation for the fluid dynamic force per density F/ρ acting on the body using a flux equation formulation given in Equation 1, with the goal of analyzing time dependent loads on bodies using only the velocity fields and their derivatives in the boundary of the domain:

$$\frac{F}{\rho} = \oint_{S(t)} \hat{n} \cdot \gamma_{flux} \, dS - \oint_{S_{b(t)}} \hat{n} \cdot [(u - u_S)u] \, dS - \frac{d}{dt} \oint_{S_{b(t)}} \hat{n} \cdot (ux) \, dS, \tag{1}$$

where T is the viscous stress tensor

$$T = \mu(\nabla u + \nabla u^T) \tag{2}$$

and with γ_{flux}:

$$\begin{aligned} \gamma_{flux} = {} & \frac{1}{2}u^2 I - uu - \frac{1}{N-1} u(x \cdot \Omega) + \frac{1}{N-1} \Omega(x \cdot u) \\ & - \frac{1}{N-1}\left[\left(x \cdot \frac{\delta u}{\delta t}\right) I - x \frac{\delta u}{\delta t} + (N-1) \frac{\delta u}{\delta t} x\right] \\ & + \frac{1}{N-1}[x \cdot (\nabla \cdot T) I - x(\nabla \cdot T)] + T. \end{aligned} \tag{3}$$

As the data from the PIV measurements have been taken using phase locked averaging, the equations have been transformed to use changes in azimuthal position to calculate the time dependent forces. The phase averaged flux equation given in Equation 4 consists of three major terms.

TABLE 2 Azimuth of the blade for each case

	$\beta=+5^\circ$			$\beta=0^\circ$			$\beta=-5^\circ$		
Case label	**Aft (°)**	**Mid (°)**	**Front (°)**	**Aft (°)**	**Mid (°)**	**Front (°)**	**Aft (°)**	**Mid (°)**	**Front (°)**
$\theta=60^\circ$	56.5	61	64.5	55	60	65	55	61.5	64.5
$\theta=90^\circ$	86	91	95.5	85	91	95	85	90	95
$\theta=120^\circ$	122.1	124.6	128.6	122	125	129	122	124.5	128.5
$\theta=240^\circ$	239.5	243.5	248.5	239.5	243.5	248.5	239.5	243.5	248.5
$\theta=270^\circ$	269.5	274.5	278	270	274	278	269.8	274	278
$\theta=300^\circ$	295	299.5	303.5	294.5	299	303	293.4	299.5	301.7

Note: The cases are labeled by an approximate azimuth. Nine azimuth positions are acquired for each case, three for each of the three pitch angle cases. The results use the case label and the pitch angle to identify the case and subcase.

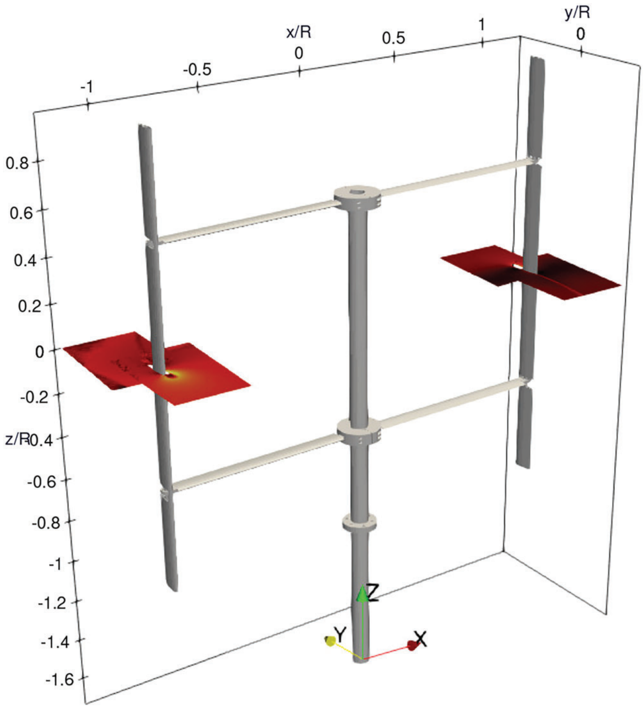

FIGURE 6 PitchVAWT turbine showing the measurement planes at locations $\theta=90$ and $\theta=270$ [Colour figure can be viewed at wileyonlinelibrary.com]

The first is the flux over the boundary surface surrounding the airfoil; this is the major target of the analysis. The next two are corrections for the inner boundary of the control volume surface. The second term has to do with flow through the boundary surface of the airfoil, as the airfoil is a solid body, this force goes to zero. The third term is due to the change of the internal boundary surface over time mainly due to the rotation of the airfoil through the control volume.

$$\frac{\langle F\rangle}{\rho}=\left\langle\oint_{S(t)}\hat{n}\cdot\gamma_{flux}dS\right\rangle_{\theta_1}-\left\langle\oint_{S_{b(t)}}\hat{n}\cdot[(u-u_S)u]dS+\frac{d}{dt}\oint_{S_{b(t)}}\hat{n}\cdot(ux)dS\right\rangle_{\theta_1} \tag{4}$$

The phase-locked average of the flux term $\langle\gamma_{flux}\rangle_{\theta_1}$ is

$$\begin{aligned}\left\langle\oint_S\hat{n}\cdot\gamma_{flux}dS\right\rangle_{\theta_1} = &\left\langle\oint_S\hat{n}\cdot\left[\tfrac{1}{2}u^2I-uu-\tfrac{1}{N-1}u(x\cdot\Omega)+\tfrac{1}{N-1}\Omega(x\cdot u)\right]dS\right\rangle_{\theta_1}\\ &-\frac{1}{N-1}\left\langle\oint_S\hat{n}\cdot\left[\left(x\cdot\frac{\delta u}{\delta t}\right)I-x\frac{\delta u}{\delta t}+(N-1)\frac{\delta u}{\delta t}x\right]dS\right\rangle_{\theta_1}\\ &+\left\langle\oint_S\hat{n}\cdot\left[\tfrac{1}{N-1}[x\cdot(\nabla\cdot T)I-x(\nabla\cdot T)]+T\right]dS\right\rangle_{\theta_1}.\end{aligned} \tag{5}$$

The instantaneous time derivative of the velocity field is approximated using multiple phase-locked azimuths offset by a $\Delta\theta$. This approximation is as follows:

$$\frac{\delta u}{\delta t} = \frac{\Delta u}{\Delta t} + O(\Delta t) = \frac{u_{\theta+\Delta\theta} - u_{\theta}}{\Delta/\omega} + O(\Delta\theta). \tag{6}$$

The full flow acceleration term can then be approximated by a numerical differentiation between nearby ($\Delta\theta$) azimuth positions.

$$\begin{aligned} &\frac{1}{N-1}\left\langle \oint_S \hat{n}\cdot\left[\left(x\cdot\frac{\delta u}{\delta t}\right)I - x\frac{\delta u}{\delta t} + (N-1)\frac{\delta u}{\delta t}x\right]dS\right\rangle_{\theta_1} = \\ &\frac{1}{N-1}\left\langle \oint_{S(t)} \hat{n}\cdot\left[\left(x\cdot\left(\frac{u_{\theta+\Delta\theta}-u_\theta}{\Delta\theta/\omega}\right)\right)I\right] + \hat{n}\cdot\left[-x\left(\frac{u_{\theta+\Delta\theta}-u_\theta}{\Delta\theta/\omega}\right) + (N-1)\left(\frac{u_{\theta+\Delta\theta}-u_\theta}{\Delta\theta/\omega}\right)\right]dS\right\rangle_{\theta_1} + O(\Delta\theta) = \\ &\frac{1}{N-1}\frac{1}{\Delta\theta/\omega}\left\langle \oint_{S(t)} \hat{n}\cdot[(x\cdot u_\theta)I - xu_\theta + (N-1)u_\theta x]dS\right\rangle_{\theta_1+\Delta\theta} \\ &-\frac{1}{N-1}\frac{1}{\Delta\theta/\omega}\left\langle \oint_{S(t)} \hat{n}\cdot[(x\cdot u_\theta)I - xu_\theta + (N-1)u_\theta x]dS\right\rangle_{\theta_1} + O(\Delta\theta). \end{aligned} \tag{7}$$

During the experiments, the turbine was operated with a constant rotational speed of 21.6 rad/s. Therefore, the term associated with the acceleration of the non-porous airfoil (third term in Equation 4 and shown explicitly in Equation 8) remains constant throughout the rotation in the reference frame of the airfoil. Therefore, the calculation of this term is independent of the azimuth position of the turbine. The force is a function of rotational velocity, the airfoil geometry, and pitch. Given the NACA0021 airfoil and the constant ω of 21.6 rad/s, the load due to the body rotation is $F_{n_b} = 0.023$ and $F_{t_b} = 0.007$, with the load non-dimensionalized by $\frac{1}{2}\rho\lambda^2 U_\infty^2 c$.

$$\frac{d}{dt}\oint_{S_{b(t)}} \hat{n}\cdot(ux)\,dS \tag{8}$$

2.5.1 | Demonstration of Noca flux equation applied to one case

As an example of the flux calculation, the azimuthal case $\theta = 120^\circ$ with a pitch of $\beta = 0^\circ$ is detailed. Each velocity field is given for $\theta = 122^\circ$, $\theta = 125^\circ$, $\theta = 129^\circ$ in Figure 7. The boundary surface, S, is shown in black for each figure. The placement of the boundary surface is based upon two criteria. The surface must be large enough to encompass the airfoil position for all three measurement locations, and there must be sufficient velocity information with accurate PIV measurement to properly calculate the terms, constricting the size of the surface. The velocities at the surfaces of $\theta = 122^\circ$ and $\theta = 129^\circ$, shown in Figure 7a,c, are used to determine the flow acceleration term given in Equation 7 by numerical differentiation over the boundary surface. The velocity, acceleration, and vorticity in term 1 of Equation 5 are given in Figures 8–10, in nondimensional

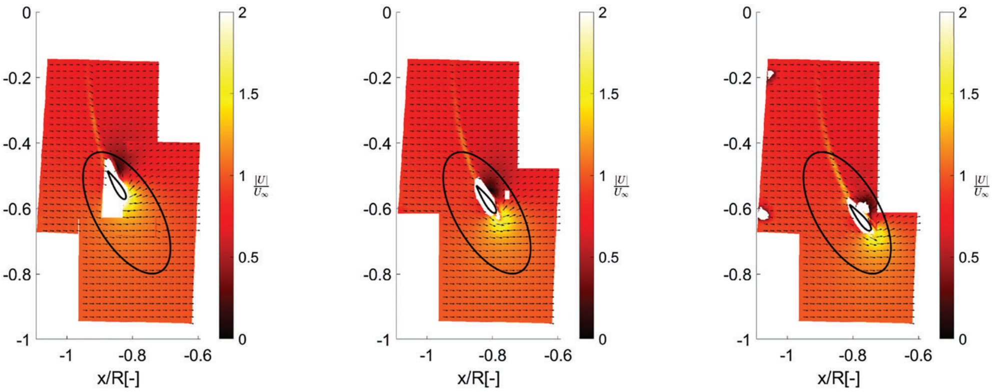

(A) $\theta = 122^\circ$ (B) $\theta = 125^\circ$ (C) $\theta = 129^\circ$

FIGURE 7 Velocity magnitude of each measurement section; the boundary surface shown as the blue oval envelopes each azimuthal position [Colour figure can be viewed at wileyonlinelibrary.com]

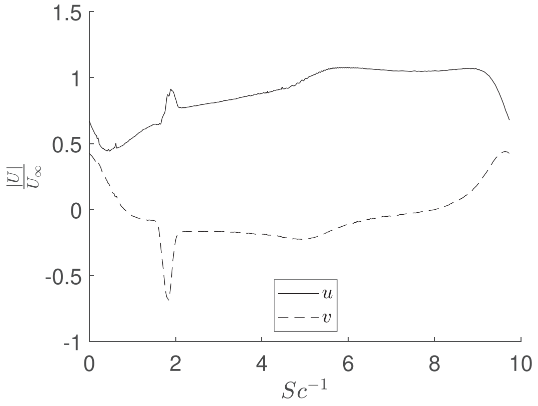

FIGURE 8 Velocity vs. distance over boundary surface

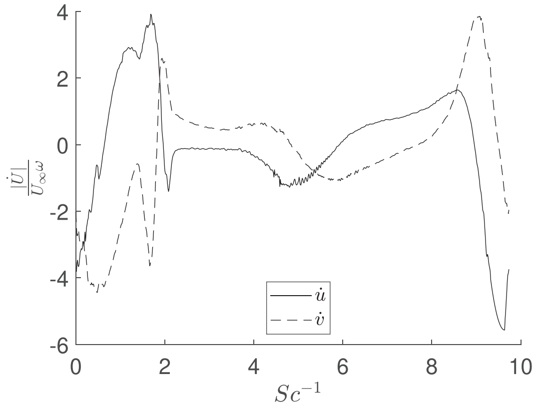

FIGURE 9 Acceleration vs. distance over boundary surface

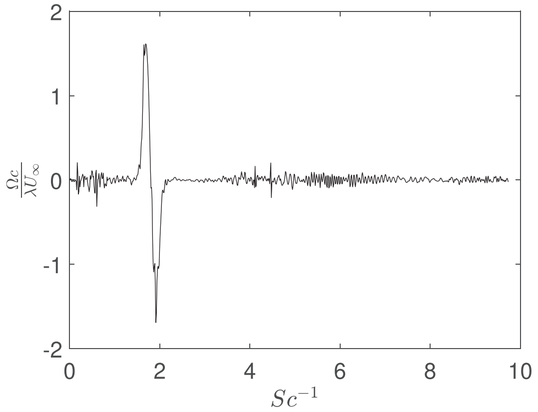

FIGURE 10 Vorticity vs. distance over boundary surface

form, respectively. The terms are plotted against the distance around the boundary surface nondimensionalized by the chord length. In the first term of Equation 5, the vorticity is multiplied by a positional vector of the integration over the boundary. In order to minimize the error associated with this moment of vorticity, the *x* positional vector is set to the location on the surface with the maximum vorticity. After subtracting out the body forces discussed in Equation 8, the load vector is calculated.

2.5.2 | Sensitivity of flux term to boundary surface

As a verification for the flux calculations detailed above, the same calculations are conducted over a variety of surfaces for the same airfoil position: one boundary surface of measured data that does not overlap the airfoil body and a series of independent surfaces which do encompass the body. The boundary surface without the body is given in Figure 11. The calculated normal and tangential force are both near 0, which is to be expected. The series of other surfaces is shown in Figure 12. The normal and tangential load was calculated for each surface. The goal is to understand the variability of calculated load based upon the boundary surface choice. The calculated loads are given in Table 3. The mean and standard deviation of the measurements are also given. For the normal load, the standard deviation is 1.6% of the mean load, whereas the tangential load is more sensitive, with a standard deviation of 16.67% of the mean load. The error likely stems from difficulty in measuring the exact momentum

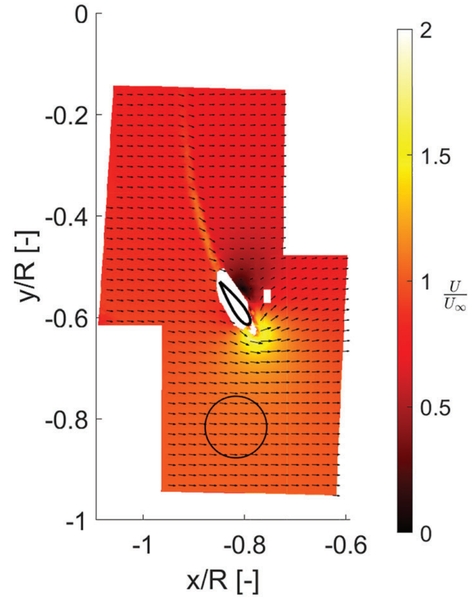

FIGURE 11 Velocity magnitude at $\theta = 125°$ with a test boundary surface not encompassing the airfoil. $F_n = 1.8e-3$, $F_t = 3.48e-4$ [Colour figure can be viewed at wileyonlinelibrary.com]

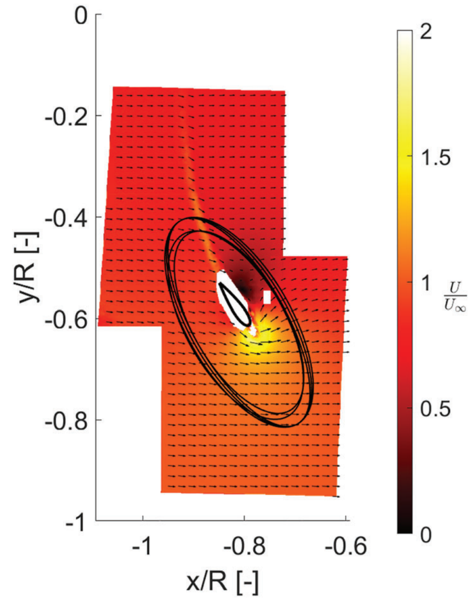

FIGURE 12 Various surface boundaries encompassing the airfoil positions. Results given in Table 3 [Colour figure can be viewed at wileyonlinelibrary.com]

TABLE 3 Sensitivity to flux surface nondimensionalized by $1/2\rho\lambda^2 U_\infty^2 c$

Surface	$F_{n_{flux}}$ [−]	$F_{t_{flux}}$ [−]
1	0.791	0.135
2	0.801	0.095
3	0.783	0.128
4	0.766	0.130
5	0.774	0.154
Mean	0.783	0.128
σ	0.014	0.021

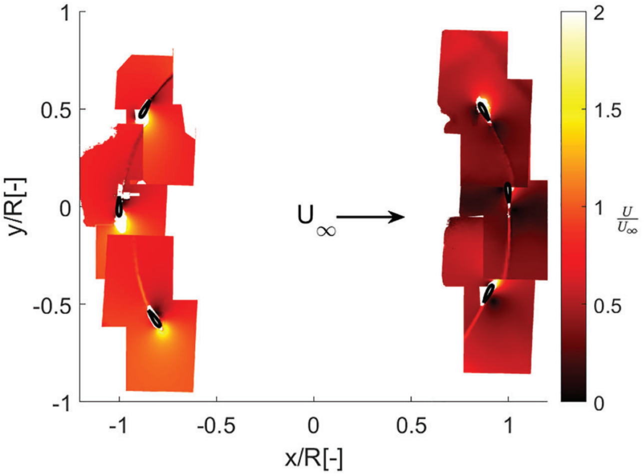

FIGURE 13 Velocity magnitude with a $\lambda = 4$ and $\beta = 0$ [Colour figure can be viewed at wileyonlinelibrary.com]

deficit and vorticity within the thin wake of the airfoil due to averaging over many rotations with slight phase offsets in the PIV measurements. This also explains the larger error for the tangential loading, as the loading in this direction is highly dependent upon the characterization of the wake.

3 | RESULTS AND DISCUSSION

3.1 | PIV velocity fields

In this section, flow fields are displayed for each of the measurement stations with fixed pitch configurations of, $\beta = 0$, $\beta = 5$, $\beta = -5$. The flow fields are presented in two sections. First, composite images showing the velocity magnitude and vorticity are given for each pitch condition at each measurement location on the rotor. Second, a closer view of the velocity magnitude and each component will be given for a subset of rotational positions.

3.1.1 | Zero pitch

The velocity fields at each azimuthal position for the zero pitch configuration are given in Figure 13. The airfoils are also plotted for reference at each position. The wind comes from the 90° position, or the left of the image, and flows in the direction of the arrow. There are several things to note in these velocity fields, starting with the overall effect of the turbine thrust slowing the flow in the downwind half of the turbine. When the blade is at a position of 270°, the effect of tower shadow is evident. On the airfoil scale, as is expected, the wake of the blade pass is evident in each of the measurement positions, as is the flow acceleration over the airfoil surface. The wake is most easily seen while looking at the vorticity

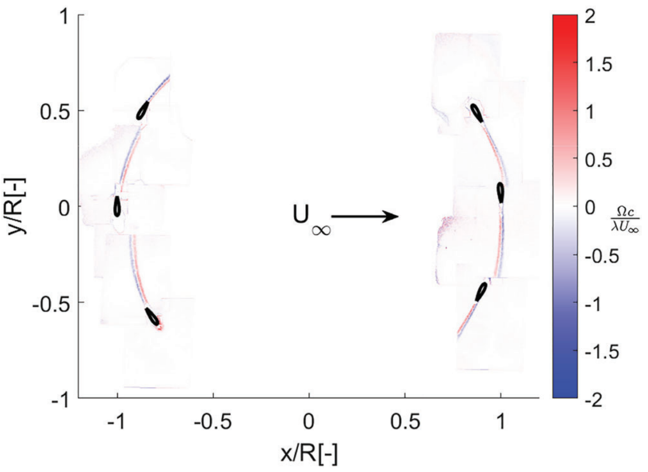

FIGURE 14 Vorticity with a $\lambda = 4$ and $\beta = 0$ [Colour figure can be viewed at wileyonlinelibrary.com]

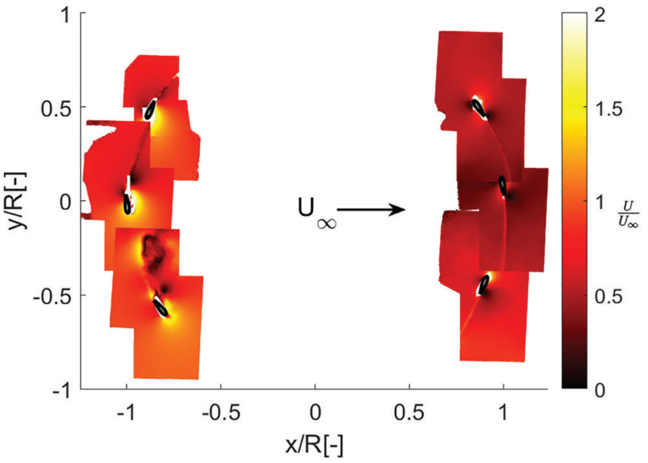

FIGURE 15 Velocity magnitude with a $\lambda = 4$ and $\beta = 5$ [Colour figure can be viewed at wileyonlinelibrary.com]

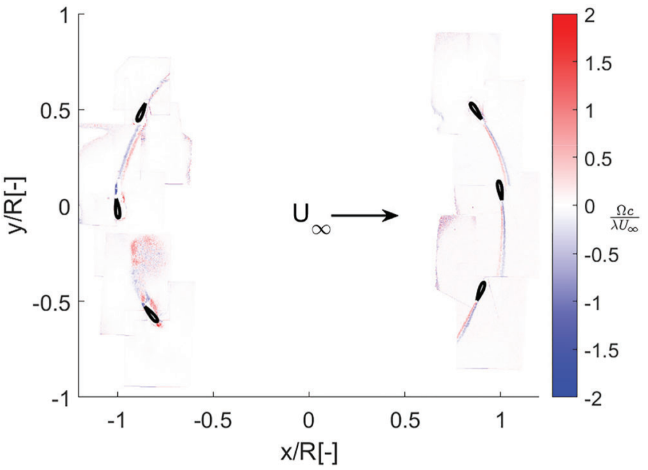

FIGURE 16 Vorticity with a $\lambda = 4$ and $\beta = 5$ [Colour figure can be viewed at wileyonlinelibrary.com]

of each measurement given in Figure 14. As can be verified, in the velocity fields as well, there may be some small laminar flow separation due to the low Reynolds number effects, but there is no clear deep stall present in this operational configuration.

3.1.2 | Five pitch

The pitch of the turbine was then commanded to 5°, toe-in, on each blade, and the PIV data were collected once again. The effect of pitching the blades in this manner causes a positive angle of attack shift which while neglecting airfoil viscous effects means a shifting of the load from the downwind to the upwind half of the rotor sweep. However, due to the airfoil stalling, a case of dynamic stall is captured. Figures 15 and 16 show the velocity and vorticity of the measurement views. Starting at the 60° position, there is a much greater flow acceleration over the airfoil as compared to the 0° pitch case, as the blade progresses to the 90° position the flow begins to separate, and by the 120° position, a large bubble has been shed into the wake of the blade. The overall velocities on the downwind half of the rotor pass are higher in the 5° pitch case than was exhibited in the 0° case above due to the stall on the upwind pass. The vorticity in the airfoil wake at each position is also less intense due to the effective angle of attack in the downwind half being reduced.

3.1.3 | Minus five pitch

In the -5° pitch case, the loading is shifted opposite from that in the 5° case discussed in the previous section. The loading is tended to shift to the downwind half of the rotor, thereby decreasing the effective angle of attack and energy extraction in the upwind half and increasing it in the downwind half. As can be seen in the velocity profiles in Figure 17, the overall wind speed entering the rotor in the upwind pass is closer to that

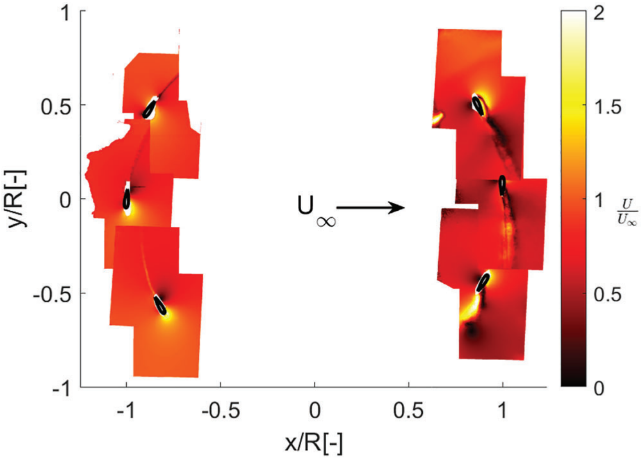

FIGURE 17 Velocity magnitude with a $\lambda = 4$ and $\beta = -5$ [Colour figure can be viewed at wileyonlinelibrary.com]

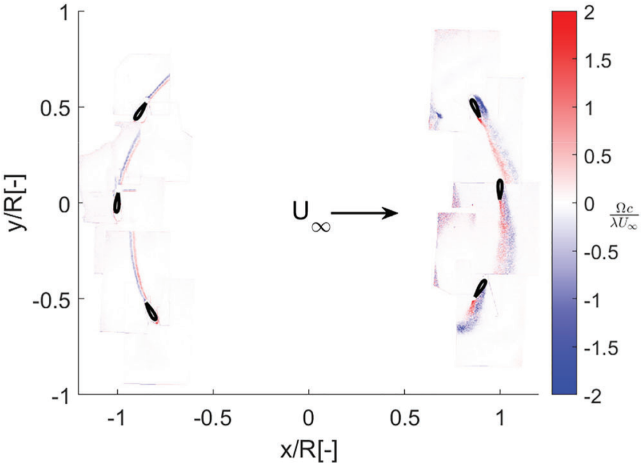

FIGURE 18 Vorticity with a $\lambda = 4$ and $\beta = -5$ [Colour figure can be viewed at wileyonlinelibrary.com]

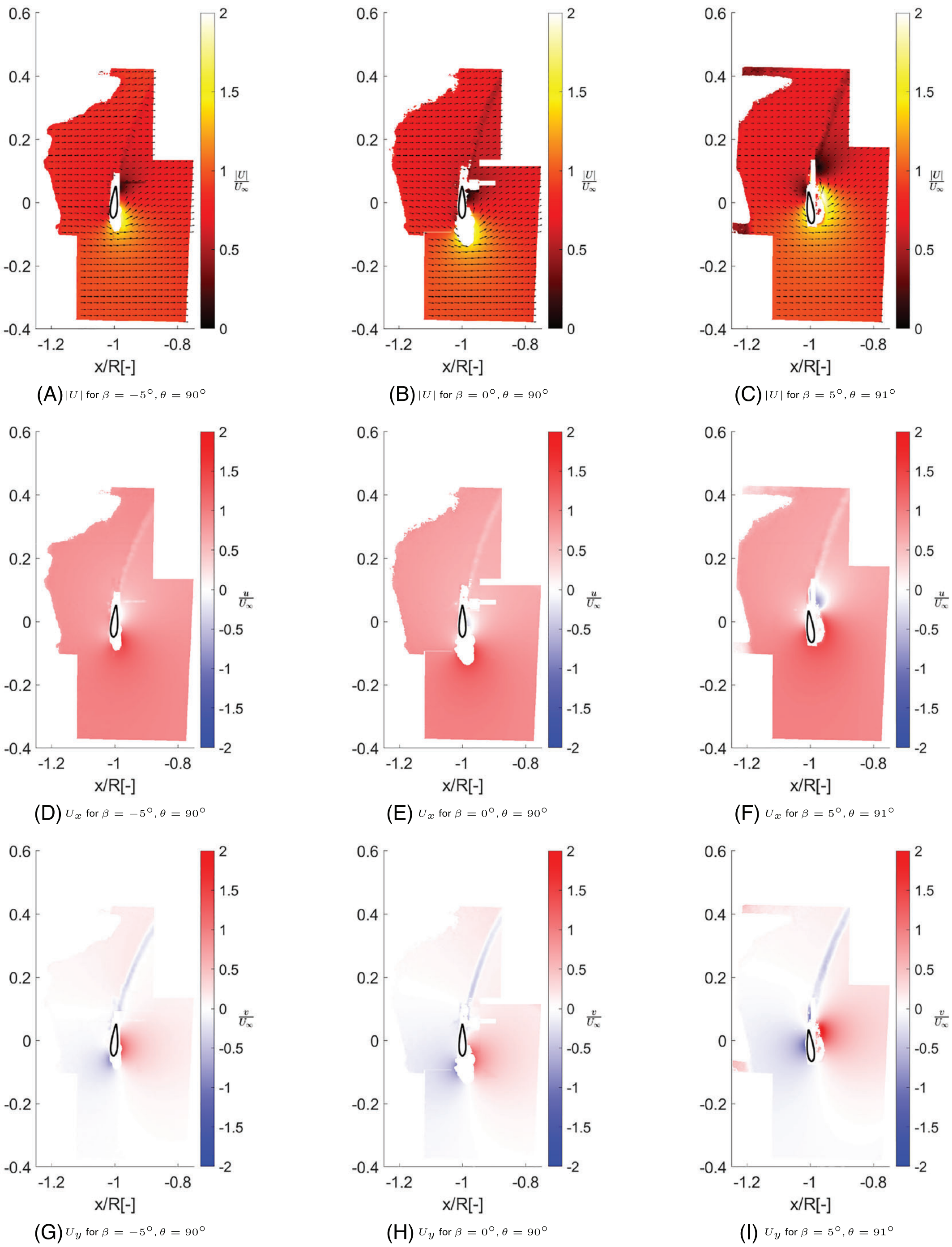

(A) $|U|$ for $\beta = -5^\circ, \theta = 90^\circ$
(B) $|U|$ for $\beta = 0^\circ, \theta = 90^\circ$
(C) $|U|$ for $\beta = 5^\circ, \theta = 91^\circ$
(D) U_x for $\beta = -5^\circ, \theta = 90^\circ$
(E) U_x for $\beta = 0^\circ, \theta = 90^\circ$
(F) U_x for $\beta = 5^\circ, \theta = 91^\circ$
(G) U_y for $\beta = -5^\circ, \theta = 90^\circ$
(H) U_y for $\beta = 0^\circ, \theta = 90^\circ$
(I) U_y for $\beta = 5^\circ, \theta = 91^\circ$

FIGURE 19 Quiver and color plot of the velocity magnitude, velocity in *x* direction, and velocity in *y* direction for $\theta = 90^\circ$ position [Colour figure can be viewed at wileyonlinelibrary.com]

of the incoming free stream velocity, as the angle of attack in the upwind pass is much less. The flow remains relatively attached as can be expected. However, once the airfoil reaches the 240° position, the airfoil begins to enter into a deep stall, which continues through the rest of the downwind positions. The flow then reattaches between the measured 300° section and the 60° section of the next pass. The displayed vorticity in Figure 18 reinforces the stall in the downwind section. When determining the proper operating pitch position for the VAWT, it is crucial to take into account the limits of the airfoil in both positive and negative angles of attack to minimize these dynamic stall phenomena. As the load is shifted between from upwind to downwind passes, or vice versa, multiple effects can be exacerbated. For example, the blade vortex interaction occurring in the downwind pass will depend on the strength of the shed vorticity of the upwind pass.

3.1.4 | Direct comparison of pitch value on flow fields

The velocity fields in Figures 19–21 give a direct comparison for the changes in flow over the surface depending on the pitch conditions for the 90°, 120°, and 270° positions. The first row of each figure gives the overall velocity magnitude along with the overlay of the vector field; the second row provides the nondimensional velocity in the flow wise, or x direction; and the last row shows the flow perpendicular to the oncoming wind. Each column represents a pitch configuration in order from left to right of $\beta = -5^\circ$, $\beta = 0^\circ$, and $\beta = 5^\circ$. These azimuth positions were chosen in order to highlight the effect of loading in the most upwind condition, the stall that sets in at the 120° position for the 5° pitch orientation, and its effect on the behavior of the downwind pass. The less the loading on the upwind half of the rotation, for instance, the -5° pitch case, the greater the flow velocity on the downwind half, increasing the relative angle of attack and exacerbating the stall, causing an overall much lower

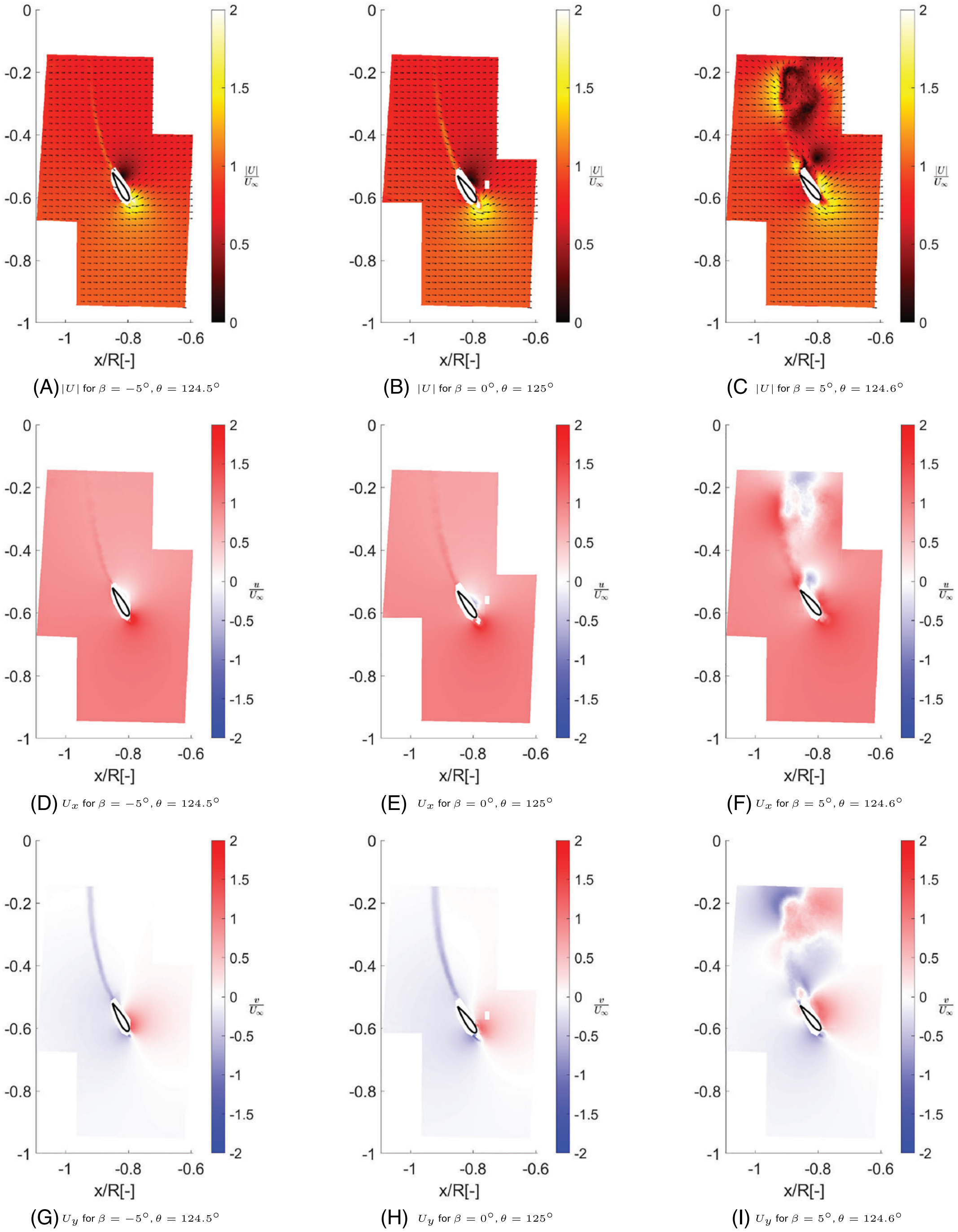

(A) $|U|$ for $\beta = -5^\circ, \theta = 124.5^\circ$ (B) $|U|$ for $\beta = 0^\circ, \theta = 125^\circ$ (C $|U|$ for $\beta = 5^\circ, \theta = 124.6^\circ$

(D) U_x for $\beta = -5^\circ, \theta = 124.5^\circ$ (E) U_x for $\beta = 0^\circ, \theta = 125^\circ$ (F) U_x for $\beta = 5^\circ, \theta = 124.6^\circ$

(G) U_y for $\beta = -5^\circ, \theta = 124.5^\circ$ (H) U_y for $\beta = 0^\circ, \theta = 125^\circ$ (I) U_y for $\beta = 5^\circ, \theta = 124.6^\circ$

FIGURE 20 Quiver and color plot of the velocity magnitude, velocity in x direction, and velocity in y direction for $\theta = 120^\circ$ position [Colour figure can be viewed at wileyonlinelibrary.com]

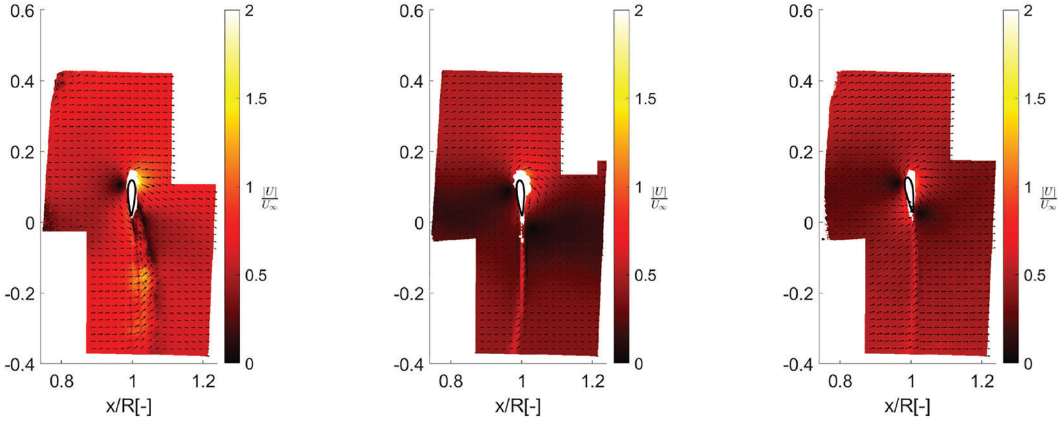

(A) $|U|$ for $\beta = -5^\circ, \theta = 274^\circ$ (B) $|U|$ for $\beta = 0^\circ, \theta = 273.5^\circ$ (C $|U|$ for $\beta = 5^\circ, \theta = 274.5^\circ$

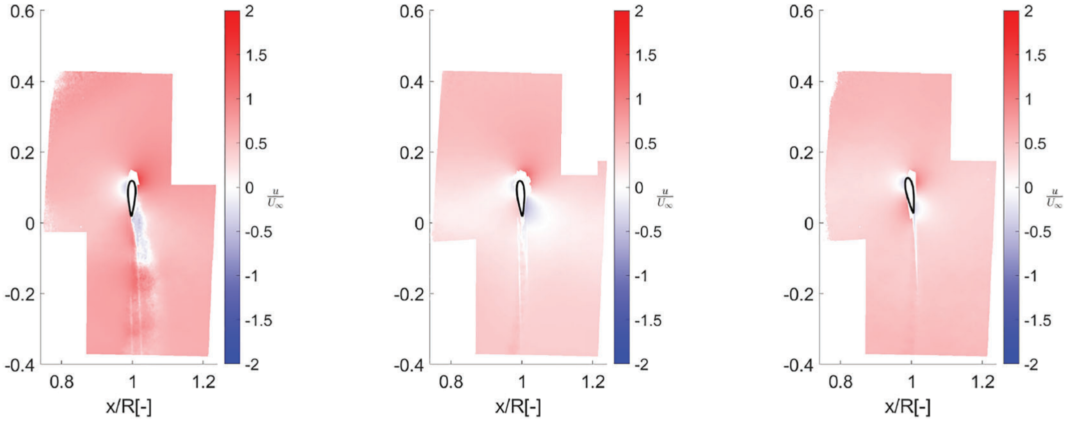

(D) U_x for $\beta = -5^\circ, \theta = 274^\circ$ (E) U_x for $\beta = 0^\circ, \theta = 274^\circ$ (F) U_x for $\beta = 5^\circ, \theta = 274.5^\circ$

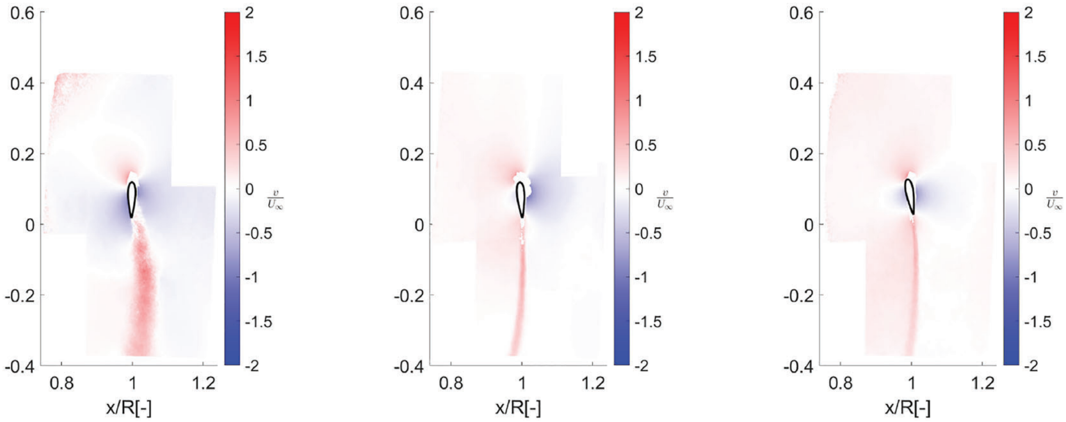

(G) U_y for $\beta = -5^\circ, \theta = 274^\circ$ (H) U_y for $\beta = 0^\circ, \theta = 274^\circ$ (I) U_y for $\beta = 5^\circ, \theta = 274.5^\circ$

FIGURE 21 Quiver and color plot of the velocity magnitude, velocity in *x* direction, and velocity in *y* direction for $\theta = 270^\circ$ position [Colour figure can be viewed at wileyonlinelibrary.com]

rotor thrust compared to the 0° pitching case. This is also exhibited in the dynamic stall seen in the 5° pitch case, causing a slightly higher velocity downwind at the 240° azimuth condition than is seen for the same pitch case at 300° azimuth.

3.2 | Load measurements from PIV

Results for the normal and tangential loading for the six azimuthal positions and the three constant pitch orientations are given in Table 4. These same results are then plotted versus the azimuth position. Figure 22 shows the normal loading, while Figure 23 gives the tangential loads at each

TABLE 4 Aerodynamic loading for each pitch configuration. The 2D loads are non-dimensionalized by $\frac{1}{2}\rho\lambda^2U_\infty^2c$

(a) $\beta = 5$			(b) $\beta = 5$			(c) $\beta = -5$		
θ [°]	F_n [−]	F_t [−]	θ [°]	F_n [−]	F_t [−]	θ [°]	F_n [−]	F_t [−]
60	1.114	0.032	61	1.672	0.122	61.5	0.401	0.046
90	1.194	0.195	91	1.538	0.120	90	1.00	0.123
125	0.791	0.135	124.6	0.324	−0.208	124.5	0.803	0.107
243.5	−0.666	0.106	243.5	−0.379	0.018	243.5	−0.358	−0.035
274	−0.667	0.069	274.5	−0.071	0.027	274	−0.256	−0.019
299	−0.740	0.074	299.5	−0.246	0.018	299.5	−0.953	−0.105

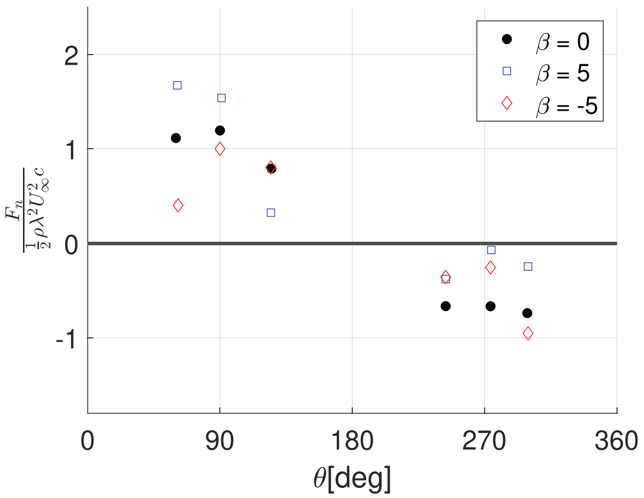

FIGURE 22 Normal load for each fixed pitch offset as given in Table 4 [Colour figure can be viewed at wileyonlinelibrary.com]

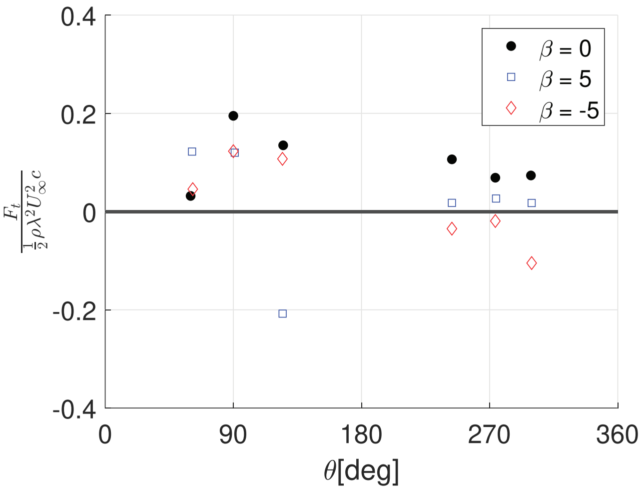

FIGURE 23 Tangential load for each fixed pitch offset as given in Table 4 [Colour figure can be viewed at wileyonlinelibrary.com]

position. A positive normal load indicates the blade reaction forces are pushing out from the normal plane of the rotor rotation, while a negative load is the opposite. Therefore, the expected upwind load is positive while the downwind normal load is negative. For tangential forces, a positive load would work to accelerate the rotor in the direction of rotation, while a negative load would work to slow the rotor. As a continuity check, the calculations were also performed from the rotating reference frame of the airfoil. This was performed by adding the local tangential velocity of

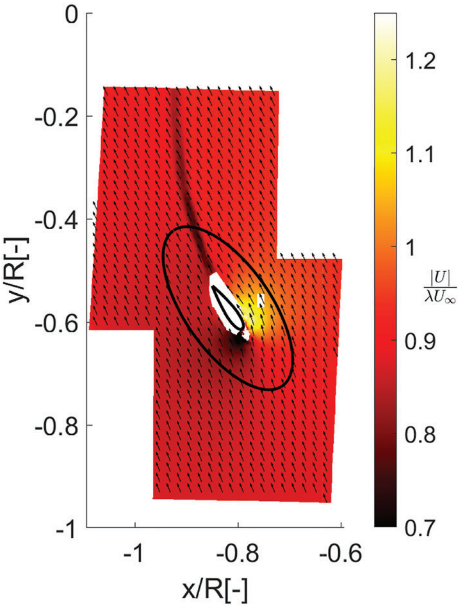

FIGURE 24 Velocity field in the airfoil reference frame at the 120° position [Colour figure can be viewed at wileyonlinelibrary.com]

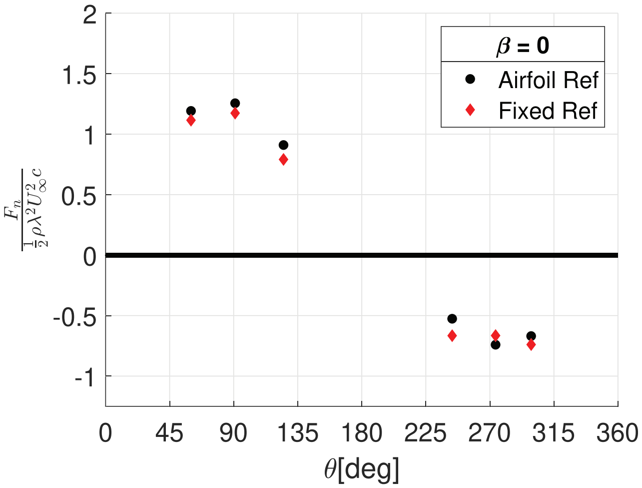

FIGURE 25 Comparison of normal load calculation in fixed and rotating reference frames [Colour figure can be viewed at wileyonlinelibrary.com]

the airfoil to the velocity fields and then moving the boundary surface with the airfoil as shown in Figure 24. The normal load calculation for each position for each reference frame is given in Figure 25. As can be seen, the two methods match well in the calculation. Each of the terms in the flux equation discussed in Equation 5, the inviscid loading term, the acceleration term, and the viscous term, can have a varying effect on the overall loading depending upon the relative values of the flow fields. The slight difference in the calculation depending on the reference frame highlights the shifting emphasis from the flow acceleration term in the fixed reference frame to a larger effect of the inviscid loading term in the rotating reference frame. The technique is quite sensitive to properly measuring the thin airfoil wake, especially for the tangential force component. In the airfoil reference frame this is complicated by having the wake change position with respect to the airfoil at each velocity field in the calculation. This effect is compounded for the airfoil reference frame with potential error added due to the approximation of adding the airfoil tangential velocity across the entire flow field of the measurement.

Data for the $\beta = 0^\circ$ pitch configuration indicates the performance of the turbine is as to be expected based upon the velocity profiles discussed above. The upwind pass shows a positive normal load and smaller torque at the 60° position peaking near 90° before declining again as the angle of attack lowers, the blade begins to move away from the oncoming wind and head to the downwind pass. At the 240° position, the loading has flipped to the other side of the airfoil, flipping the direction of the normal load. The overall loading is lower than the upwind pass due to the relative velocity in the back half of the rotor being lower. The rotor load is fairly consistent across the downwind pass, at least at this relatively coarse resolution, which has been seen in previous modeling studies of the VAWT.

With the blades pitched to $\beta = 5^\circ$, the loading becomes very interesting. As expected, the normal loading is much greater at the $\theta = 60^\circ$, and $\theta = 90^\circ$ positions due to the greater angle of attack, however, at 90° both the normal and tangential loads drop relative to the $\theta = 60^\circ$ position, indicating the onset of stall behavior. By $\theta = 120^\circ$, the airfoil has completely stalled, with the normal force dropping substantially and the tangential force dropping further from the 90° position, becoming negative. This of course follows with the massive separation event as shown in Figure 15. On the downwind half of the rotor pass, the normal load is negative, and the tangential load goes slightly positive; however, the angle of attack is decreased in magnitude from the $\beta = 0^\circ$ case causing lower overall loading. The loading for the 240° case is relatively greater than for the other downwind locations, most likely due to the flow velocity being higher there as the airfoil was stalled directly upwind of the location.

At a pitch of $\beta = -5^\circ$, the behavior is opposite of that experienced with the blades pitched positively. With a lower angle of attack on the upwind pass, the normal load is lower than the previous pitch scenarios. However, on the downwind pass, where the angle of attack is a greater magnitude, the blade goes into a deep stall, as shown in the loading by the lower magnitude normal load, and the negative tangential load. This is confirmed with the velocity field shown in Figure 17. The stall cancels out what would be expected to be a greater magnitude normal load on the downwind pass for the negative pitch value. At the $\theta = 300^\circ$ position, the flow begins to reattach, causing a spike in the normal and tangential loading.

4 | CONCLUSIONS

Experiments were conducted on a Vertical Axis Wind Turbine in multiple pitch configurations testing the effect of shifting load between upwind and downwind passes. Particle Image Velocimetry was deployed on the rotating turbine in each pitch configuration to capture velocity fields for 18 independent measurements using 54 individual velocity fields. A phase-locked averaging interpretation of the Noca method for calculation of fluid forces on a body using velocity fields and their derivatives to successfully calculate the normal and tangential loads on the blades. These measurements were consistent in two reference frames, a fixed global frame, and a reference frame rotating with the blades. The measurements highlight the effect of dynamic stall on the loading profile of the VAWT in both the upwind and downwind sections of the rotation, depending on the pitch angle. The measurements show, prior to stall, the load is shifted upwind with increasing pitch angle as to be expected; however, once the airfoil enters stall, the benefits of this increased load vanishes resulting in loss of thrust and decreased overall torque generation. The effects of stall in the upwind section of rotation cause an increased wind velocity in the downwind section, leading to higher loading in the position directly downwind of the stall. For cases of negative pitch, which shifts the load to the downwind side, the upwind pass removes little energy from the flow, leading to a higher perceived angle of attack on the downwind pass. This caused the airfoil to enter deep stall and to experience a spike of loading later in the rotation when the flow reattaches. The presented data gives insight into 2D aerodynamic loading, tower shadow, and dynamic stall behavior of the VAWT it multiple pitch configurations and can function as a benchmark to validate numerical models of the phenomena.

ACKNOWLEDGMENTS

The authors would like to acknowledge the support for this work through both the S4VAWT project within the framework of the TKI Wind op Zee program and the Arkom-Tulyp wind project which is sponsored by RVO, the Netherlands Enterprise Agency, under a sustainable energy subsidy.

NOMENCLATURE

α	angle of attack (°)
β	pitch angle (°)
S_b	surface of body
λ	tip speed ratio (−)
Ω	vorticity [s^{-1}]
ρ	fluid density (kg m^{-3})
θ	azimuthal position (°)
F	force on body (N)
I	identity matrix
N	number of spatial dimensions
S	control surface boundary
$\hat{n}$	surface normal vector
T	viscous stress tensor

u	local flow velocity (m s^{-1})
U_∞	free stream velocity (m s^{-1})
FOV	field of view
OJF	Open Jet Facility, Delft University of Technology
PIV	Particle Image Velocimetry

CONFLICT OF INTEREST

The authors declare no potential conflict of interests.

PEER REVIEW

The peer review history for this article is available at https://publons.com/publon/10.1002/we.2674.

DATA AVAILABILITY STATEMENT

The data that support the findings of this study are openly available in PitchVAWT Data at https://doi.org/10.1006/jfls.1999.0219.

ORCID

Bruce LeBlanc https://orcid.org/0000-0002-2711-2825

REFERENCES

1. Huijs F, Vlasveld E, Gormand M, et al. Integrated design of a semi-submersible floating vertical axis wind turbine (vawt) with active blade pitch control. *EERA DeepWind 2018, 15th Deep Sea Offshore Wind R&D Conference*. Trondheim, Norway: IOP Publishing Ltd; 2018:12.
2. De Tavernier D, Vire A & Ferreira C. Damping the floater motion of vertical-axis wind turbines using load optimisation. In: NAWEA WindTech. Journal of Physics Conference Series. Amherst, Massachusetts; 2020:14.
3. LeBlanc B, Ferreira C. Experimental demonstration of thrust vectoring with a vertical axis wind turbine using normal load measurements. *The science of making torque from wind (torque 2020)*. Delft, The Netherlands: IOP Publishing; 2020:11.
4. De Tavernier D, Ferreira C, van Bussel G. Airfoil optimisation for vertical axis wind turbines with variable pitch. *Wind Energy*. 2018;22(4):547-562.
5. Asztalos KJ, Rempfer D. Performance optimization for vertical-axis wind turbines with blade-element method models. *J Propuls Power*. 2020;36:10.
6. Battisti L, Persico G, Dossena V, Paradiso B, Raciti Castelli M, Brighenti A, Benini E. Experimental benchmark data for H-shaped and Troposkien VAWT architectures. *Renew Energy*. 2018;18:50.
7. Simão Ferreira CJ. The near wake of the VAWT 2D and 3D views of the VAWT aerodynamics. *Thesis*. Delft, The Netherlands; 2009.
8. Castelein D, Ragni D, Tescione G, Simão Ferreira CJ, Guanaa M. Creating a benchmark of vertical axis wind turbines in dynamic stall for validating numerical models. In: 33rd Wind Energy Symposium AIAA SciTech Forum. Kissimmee, Florida: American Institute for Aeronautics and Astronautics; 2015.
9. Castelein D. Dynamic stall on vertical axis wind turbines, creating a benchmark of VAWTs in dynamic stall for validating numerical models. *Thesis*. Delft, The Netherlands; 2015.
10. Greenblatt D, Ben-Harav A, Mueller-Vahl H. Dynamic stall control on a vertical-axis wind turbine using plasma actuators. *AIAA J*. 2014;52(2).
11. Edwards J, Danao LA, Howell R. PIV measurements and CFD simulation of the performance and flow physics of a small scale vertical axis wind turbine. *Wind Energy*. 2013;18(2):201-217.
12. Tescione G, Ragni D, He C, Simão Ferreira CJ, van Bussel GJW. Near wake flow analysis of a vertical axis wind turbine by stereoscopic particle image velocimetry. *Renew Energy*. 2014;70:47-61.
13. del Campo V, Ragni D, Micallef D, Akay B, Diez FJ, Simão Ferreira CJ. 3D load estimation on a horizontal axis wind turbine using spiv. *Wind Energy*. 2013;17(11):1645-1657.
14. del Campo V, Ragni D, Micallef D, Diez FJ, Simão Ferreira CJ. Estimation of loads on a horizontal axis wind turbine operating in yawed flow conditions. *Wind Energy*. 2014;18(11):1875-1891.
15. LeBlanc BP, Ferreira CS. Overview and design of PitchVAWT: vertical axis wind turbine with active variable pitch for experimental and numerical comparison. In: AIAA SciTech ForumWind Energy Symposium. Milan, Italy: American Institute of Aeronautics and Astronautics; 2018:11.
16. LeBlanc BP, Ferreira CS. Experimental determination of thrust loading of a 2-bladed vertical axis wind turbine 1037. The Science of Making Torque from Wind. Journal of Physics Conference Series; 2018:9.
17. Noca F, Shiels D, Jeon D. Measuring instantaneous fluid dynamic forces on bodies, using only velocity fields and their derivatives. *J Fluids and Struct*. 1997;11(3):345-350.
18. LeBlanc B, Ferreira C. Pitchvawt data. https://doi.org/10.4121/c.5287879; 2021.
19. Noca F, Shiels D, Jeon D. A comparison of methods for evaluating time-dependent fluid dynamic forces on bodies, using only velocity fields and their derivatives. *J Fluids Struct*. 1999;13(5):551-578.
20. Ferreira C, van Bussel GJW, van Kuik GAM, Scarano F. On the use of velocity data for load estimation of a VAWT in dynamic stall. *J Solar Energy Engineering*. 2011;133:8.

AUTHOR BIOGRAPHIES

Bruce LeBlanc is a PhD researcher in the Wind Energy research group at the Delft University of Technology. His current research focuses on the structural dynamic and aerodynamic response of vertical axis wind turbines. Bruce has Bachelor and Masters degrees in Mechanical engineering with a focus on structural dynamics and sensor systems.

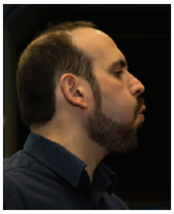

Prof. Carlos Ferreira holds the Chair in Wind Energy Science at Delft University of Technology. He has researched VAWT aerodynamics since 2004 with several publication in the topic.

How to cite this article: LeBlanc B, Ferreira C. Estimation of blade loads for a variable pitch vertical axis wind turbine from particle image velocimetry. *Wind Energy*. 2021;1-20. doi:10.1002/we.2674